X-RAY PULSAR MODELS. II. COMPTONIZED SPECTRA AND PULSE SHAPES

P. MÉSZÁROS
Astronomy Department, Pennsylvania State University

AND

W. NAGEL
Max-Planck-Institut für Physik und Astrophysik, Institut für Astrophysik
Received 1985 March 18; accepted 1985 June 3

ABSTRACT

We calculate pulse shapes and spectra for various X-ray pulsar models, including simple self-emitting or externally illuminated slabs and columns. We use a discrete-ordinate transfer scheme with eight angles × 32 frequencies × 2 polarizations and ignore bulk motions and inhomogeneities. With these simplifications, the calculated pulse shapes, cyclotron profiles, and continua as a function of phase angle are compared against observations. This indicates that slab models are in better general agreement with observations than column models. The injection of soft photons at $\hbar\omega_s \lesssim 1$ keV seems required to explain the power law continuum. The possibility of determining the cyclotron energy by means of the pulse shapes is discussed.

Subject headings: pulsars — radiative transfer — stars: neutron — X-rays: binaries

I. INTRODUCTION

In our previous work (Mészáros and Nagel 1985, hereafter Paper I), we investigated the spectra of magnetized slabs and columns, using a Feautrier discrete ordinate scheme, supplemented by an approximate transfer scheme. Generalized boundary conditions were used to investigate self-emitting and externally illuminated atmospheres, and a discrete four-angle grid with 32 frequencies × two polarizations allowed a preliminary study of the pulse-phase dependence of the cyclotron profile and the continuum. In the present paper, we investigate the pulse shapes and obtain a more detailed description of the phase-dependent spectral properties. A denser angle grid is required, and here we utilize eight angles. Under the simplifying assumption that the magnetic and rotation axes are both centered, the pulses are symmetric, so that one has 16 points to cover the phase region $0 \leq \phi \leq 1$. Knowing the basic features of various atmosphere types from the more restricted calculation of Paper I, and having to some degree investigated parameter space there, we can here concentrate on some of the most typical models.

We investigate here in particular the self-emitting slabs and cylinders of small and large effective optical depth, and the slab illuminated from the outer boundary by external soft photon sources. The self-emitting atmospheres are a good testing ground for cyclotron line profile effects and for investigating variations at $\hbar\omega \gtrsim kT_e$ which are only due to the choice of geometry. However, as discussed in Paper I, they do not reproduce observed spectra below $\hbar\omega \lesssim 3$–5 keV, since they have a low-energy thermal turnover due to self-absorption. On the other hand, low-density models (compatible with free-fall densities), which have an additional external source of soft (< 1 keV) photons, seem to fit the observed spectra fairly well even at low frequencies. In addition, the phase variation of the blue wing of the cyclotron line suggests that the geometry may be of the slab type (i.e., plane parallel with $\boldsymbol{B}$ perpendicular to the surface), on which we here concentrate.

II. PROCEDURE AND MODELS

As in Paper I, we use a magnetic field of 3.3×10^{12} G, with cyclotron frequency at $\hbar\omega_B = 38$ keV. The temperatures used satisfy $kT < \hbar\omega_B$, so that transitions to levels higher than $n = 1$ can be neglected. The photon creation mechanism used is e-p bremsstrahlung, which includes the cyclotron resonance line photon creation; and the inverse mechanism provides for absorption. Nonrelativistic cross sections are used, with first-order relativistic and quantum corrections, including vacuum polarization. In the differential scattering cross section, both Comptonization and recoil effects are included; thus partial redistribution effects are taken into account. The redistribution matrix therefore is an $N \times N$ array, each N being a channel (a particular angle, frequency, and polarization) with a certain probability of making a transition to another channel. Here $N = N_A N_F N_P$, where $N_A = 8$, the number of angles, $N_F = 32$, the number of frequencies, and $N_P = 2$, the number of normal polarization modes. The matrix is therefore of dimension $N \times N = 512 \times 512$. The code as written requires about 11 Mbytes of core memory, which was not available at the time of our earlier calculations of Paper I. Experiments were made to see if the number of angles could be increased at the expense of the number of frequencies, which indicated that anything less than about 25–30 frequencies, over a range of 2–2.5 decades, would have introduced numerical errors in the frequency changes (Comptonization). We continued, therefore, to use 32 frequencies.

The choice of the angle quadrature scheme determines the discrete values of the angle grid. Here we used a simple Gaussian method, with $\mu_i = \cos \theta_i$ as the independent variable distributed between 0 and 1, $\mu_1, \ldots, \mu_8$. This choice of scheme has the advantage of introducing the least numerical error in the evaluation of the angle integrals of, e.g., the differential scattering cross section (as checked against optical theorem values). It has the property that the smallest angle is about 11°, while the largest is about 89°. Other schemes, e.g., a Gaussian

138

scheme for the second moment of μ, would shift the angle points to somewhat lower values but give less accuracy in the optical theorem check, so we opted for the simple Gaussian scheme described first.

The calculations assume a static, homogeneous atmosphere. In the slab, there is a uniform magnetic field perpendicular to the surface, and in the column, the field is parallel to the surface, along the axis. Thus, any cyclotron line changes with angle of frequency are strictly due to viewing angles or the scattering kinematics in the plasma rest frame.

In the absence of external photon sources, the plasma parameters chosen are $kT = 8$ keV, $\hbar\omega_B = 38$ keV, and $\rho = 0.5$ g cm^{-3}. This density provides the "typical" luminosity $L_x \approx 10^{37}$ ergs s^{-1} for a "typical" external emitting surface A of about a few times 10^{10} cm^2. An atmosphere depth of $y = 50$ g cm^{-2} ($R = 10^2$ cm at this density) may be typical of Coulomb decelerated atmospheres in the slab case (Harding *et al.* 1984). The self-emitting slab and column of $R = 10^2$ cm are models B and C in our discussion. For this depth, the thermalization depth of photons is comparable to or larger than the plasma dimension along the space coordinate.

A second set of models consists of a self-emitting slab (E) and column (D) of optical depth $y = 5 \times 10^4$ g cm^{-2}, or $R = 10^5$ cm, keeping the other plasma parameters the same. For these models, the thermalization depth of photons at all frequencies is less than the plasma spatial dimension, i.e., the plasma achieves thermal equilibrium in the inner region.

A third model considered, F, is a slab model illuminated from the outer boundary by an external soft photon source ($E_s < 1$ keV). The plasma parameters in this case are $kT = 7$ keV, $\hbar\omega_B = 38$ keV, and $\rho = 1.67 \times 10^{-4}$ g cm^{-3}. The density is typical of free-fall or post-shock conditions for an accretion rate near critical. The soft photon source is taken to have a blackbody spectrum of $T_{bb} = 0.1$ keV but intensity a factor of 10^4 higher than for a blackbody of 0.1 keV, i.e., some kind of nonthermal source, or else a source of radiation temperature rather less than the kinetic temperature. For this low-density atmosphere, the hard X-ray luminosity consists of upscattered soft photons, and this input soft luminosity gives an output $L_x \approx 10^{37}$ ergs s^{-1} if the outer area of the hot atmosphere is A about a few times 10^{10} cm^2. As in Paper I, we do not pursue the nature of this soft source (cf., however, Bussard, Mészáros, and Alexander 1985) but rather look at its effects and implications in the medium to hard X-ray range.

III. SPECTRUM FORMATION

In this section we describe the emergent spectrum and the interior photon density, as calculated with the Feautrier method. We consider first the atmospheres with purely thermal photon sources (no external illumination), starting with the case of a relatively shallow depth, $y = 50$ g cm^{-2}, representing a linear depth of $R = 10^2$ cm (Thomson optical depth $\tau_T = 20$). The inner boundary condition is one of perfect reflection, and the outer one assumes no incoming radiation from outside. Run B is for a slab, and run C is for a column. Then we discuss the same for $y = 5 \times 10^4$ g cm^{-2}, or $R = 10^5$ cm, which are runs E (slab) and D (column). The polarization convention used here agrees with that in Mészáros, Nagel, and Ventura (1980). At low frequencies $\omega \ll \omega_{v1} = 3(n_e/10^{22})^{1/2}(4.4 \times 10^{12}/B)$ keV, the polarization 1 used here agrees with the usual ordinary, and 2 with the usual extraordinary (i.e., reversing the usual convention). Figure 1a shows the angle-integrated spectrum for the thin slab. Squares are polarization

1, circles are 2, and the triangles are the total. The cyclotron line is seen as a negative feature in polarization 2, while in polarization 1 (more dominant at this frequency and in the total) it appears only as a smooth shoulder. This is further illustrated in Figure 1b, which gives the total differential flux summed over both polarizations, $F_\omega(\theta) = I_\omega(\theta) \cos\theta$ (slab), for the eight different angles, $88°8$, $84°2$, $76°3$, $65°9$, $53°7$, $40°3$, $26°1$, and $11°4$, represented by square, circle, triange, plus, cross, diamond, arrow, and closed cross symbols respectively. For the slab, the differential flux increases with decreasing angle, since $\cos\theta$ is smallest for $88°8$ (limb darkening) and largest for $\theta = 11°2$, close to perpendicular to the surface (and close to parallel to the field B_0). In order to separate the curves better, we have multiplied them by successive factors of $10^{-1/2} = 0.3162...$, except for the smallest angle (*closed cross*). Thus $F(11°)$, which is the top curve, shows the true value, $F(26°)$, next lower, is true value times $10^{-1/2}$, $F(40°)$ is true value times 10^{-1}, etc. The lowest curve, $F(89°)$ is true value times (3.162×10^{-4}). The two smallest angles of propagation are close enough to the field direction to introduce significant Doppler broadening,

$$\left(\frac{\Delta\omega}{\omega_B}\right)_{\text{FWHM}} = \left(\frac{8 \ln 2 kT_e}{m_e c^2}\right)^{1/2} \cos\theta , \qquad (1)$$

which smooths the resonance out. These two lowest values of the discrete angle grid dominate the angle integral of polarization 1 and the total, as seen in Figure 1a. The resonance is, however, deeper in polarization 2, even at small angles, so that after integrating over angles the line is fairly pronounced in polarization 2. Note that, in this convention, for frequencies above the vacuum frequency defined in Paper I, $\omega_{v1} \approx 10$ keV, polarization 2 coincides (as far as direction of electric vector oscillation) with the "usual" ordinary (cf. Mészáros and Ventura 1979; Pavlov, Shibanov, and Yakovlev 1980), that is, the electric vector is mainly parallel to the magnetic field, or rotating opposite to the sense of an electron's gyration.

In Figure 2 we show the corresponding angle-integrated and differential flux from the thin column. Here the cyclotron line is more evident, even in the integrated spectrum, since now the differential flux is $F(\theta) = I(\theta) \sin\theta$ (cylinder) and the largest contributions come from large angles (i.e. 89°), close to perpendicular to B_0, where the Doppler broadening (1) is minimal. In the column case the limb darkening effect is in opposite direction to that in the slab and appears less pronounced than in the slab case. In Figure 2b one must remember that the same $10^{-1/2}$ progressive offset factor has been included but in the opposite sense. That is, $F(89)$ is now true value, $F(84)$ is true value times $10^{-1/2}$, etc. Even without it, the curve for 89° is the most intense, and successive ones progressively lower. The less pronounced limb darkening is due, partly, to the angle grid chosen, based on $\cos\theta$, which gives greater weight to larger angles. More importantly, it is due to the fact that the opacities decrease, at $\omega < \omega_B$, as the angle of propagation decreases toward the field direction. The net intensity $I_\omega(\theta)$ tends to increase towards low θ, due to this decrease in opacity, which offsets the decrease in the $\sin\theta$ factor entering the flux.

The large optical depth runs, with $R = 10^5$ cm or $y = 5 \times 10^4$ g cm^{-2}, models E (slab) and D (column) are shown in Figures 3 and 4. They differ in details from the low-depth B and C runs, but not in the qualitative sense. This is not surprising since τ_T is 20 and 2×10^4 for the low and high depth models respectively, i.e., $\tau_T \gg 1$ in both cases. The direction-
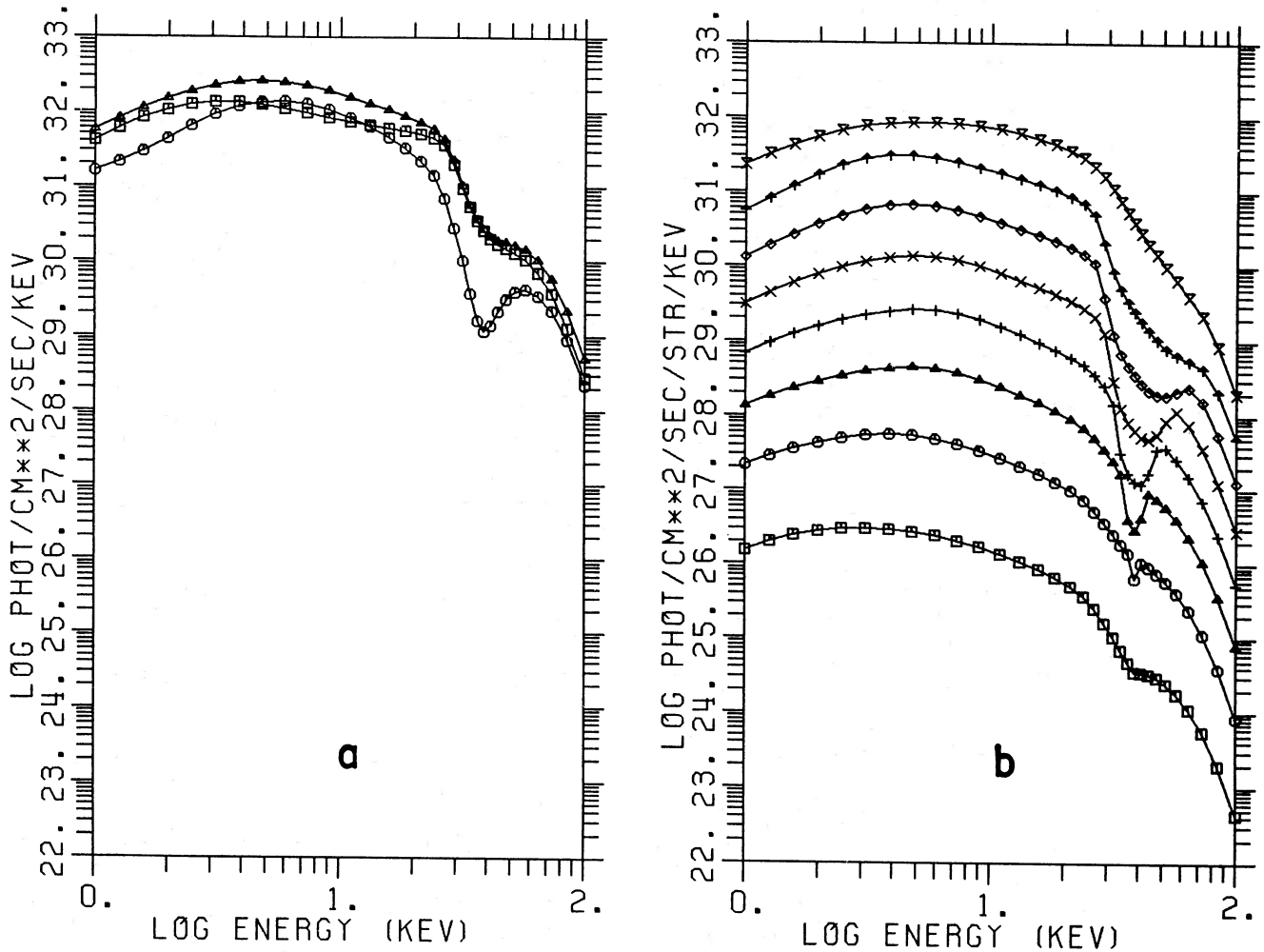
FIG. 1.—Model B, a slab of $\rho = 0.5$ g cm^{-3}, $kT = 8$ keV, $\hbar\omega_B = 38$ keV, $R = 10^2$ cm, magnetic field perpendicular to the surface. (a) Flux integrated over angle. *Squares*, polarization 1; *circles*, polarization 2; *triangles*, 1 plus 2. (b) Differential flux $I_\omega(\theta) \cos \theta$, (1 and 2), for the eight angles 89°, 84°, 76°, 66°, 54°, 40°, 26°, 11° (squares, circles, triangles, plusses, crosses, diamonds, arrows, and closed crosses respectively). Uppermost curve (11°) for slab shows the actual value, successive curves of increasing angle are staggered by increasing powers of $10^{-1/2}$, in order to separate them (see text).

ality and general spectral index of the escaping radiation are not expected to differ much. However, the thermalization and mixing length λ_t and λ_m (see eqs. [2] and [3] and discussion below) are rather different in the two cases, so that the total number of photons produced and their distribution inside the atmosphere are different. The main observational difference between the two depth cases originates from the larger amount of escaping photons in the deeper case. As a consequence, runs E and D show an increased flux near $\hbar\omega \approx 3kT_e = 24$ keV, caused by an increased number of both lower and higher frequency photons which have accumulated near the Wien peak

corresponding to $kT_e = 8$ keV, the atmosphere's temperature. The power (ergs cm^{-2} s^{-1}) in polarization 1, 2, and total are shown in Table 1. As seen in Table 1, the total power for a thin slab is somewhat larger than for the thin column. This is because in this case the thermalization length is large compared to the radius of the column, which allows photons to escape from a column after fewer scatterings than from a slab of the same depth. For the deep slabs and columns, however, the thermalization depth is small compared to the depth, or radius of the atmosphere, so that both are essentially plane parallel. However, in the slab, the limb darkening is more pronounced than in the columns, as discussed above, so that the total emergent flux is somewhat less from the deep slab than from the deep column.

An "effective" thermalization depth at various frequencies can be seen in plots of the photon density (photons cm^{-3} keV^{-1}) as a function of atmosphere depth. These plots are shown separately for polarizations 1 and 2 in Figures 5a and 5b for the thin slab (B) and 6a and 6b for the deep slab (E). The selected frequencies shown are 1.58, 3.85, 8.98, 18.37, 29.13, 38.59, 51.71, and 84.66 keV, with symbols of a square, circle, triangle, plus, cross, diamond (cyclotron frequency), arrow, and closed cross. Comparing corresponding plots for slabs and

TABLE 1

POWER
(ergs cm^{-2} s^{-1})

POLARIZATION	MODEL			
	B	C	E	D
P_1	4.42×10^{25}	3.04×10^{25}	1.09×10^{26}	1.12×10^{26}
P_2	2.70×10^{25}	2.39×10^{25}	6.60×10^{25}	1.17×10^{26}
P_T	7.12×10^{25}	5.43×10^{25}	1.75×10^{26}	2.29×10^{26}
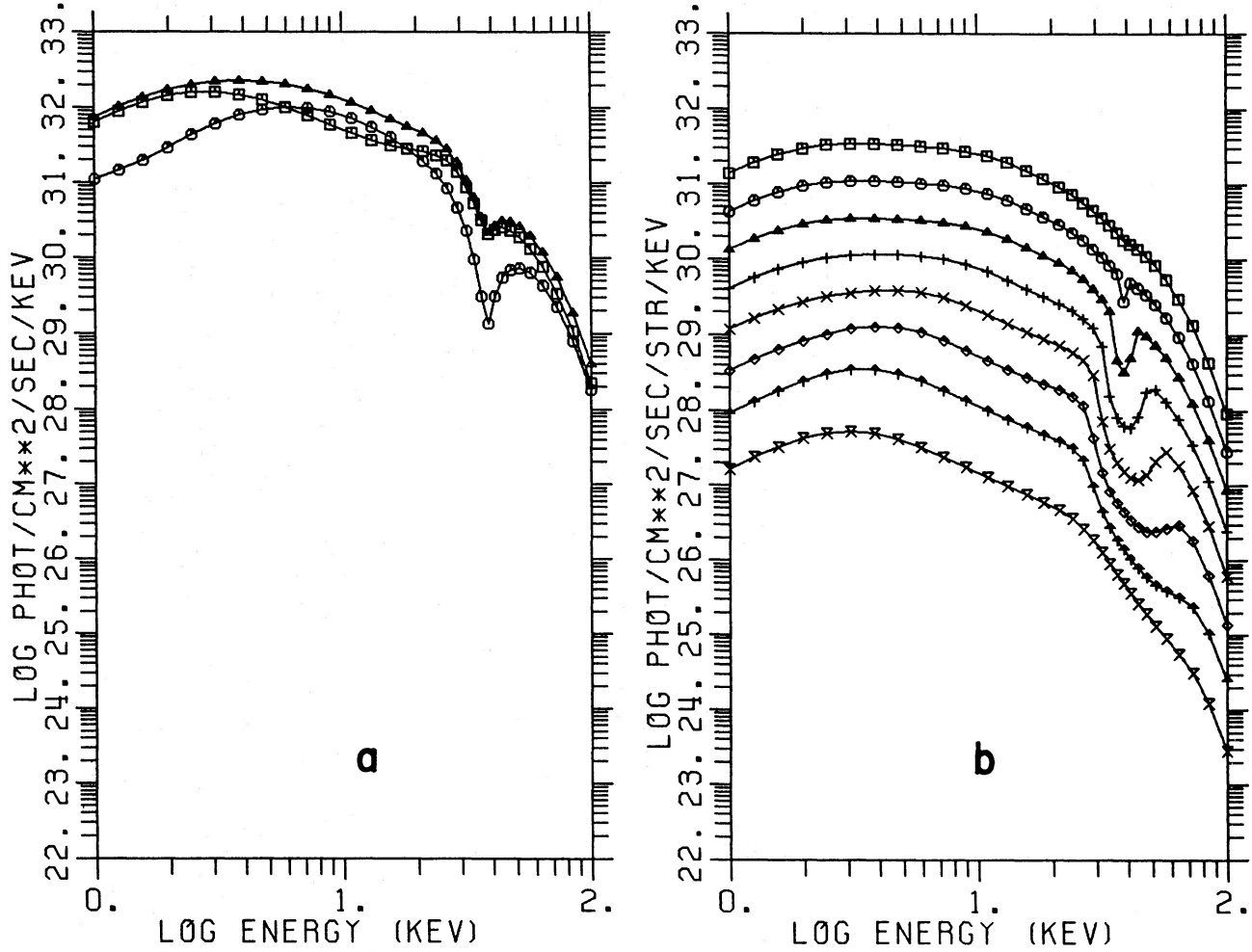
Fig. 2.—Model C, a column of $\rho = 0.5$ g cm^{-3}, $kT = 8$ keV, $\hbar\omega_B = 38$ keV, $R = 10^2$ cm, magnetic field parallel to the surface. (a) Flux integrated over angle, symbols as in Fig. 1. (b) Differential flux $I_\omega(\theta)$ sin θ, (1 and 2), for the same eight angles labeled by the same symbols as in Fig. 1. Uppermost curve here is 89°, shown at true value, and each successive curve of decreasing angle is staggered by increasing powers of $10^{-1/2}$ (see text).

cylinders (not shown) confirms the slight excess of photon density, and hence flux, of a slab with respect to the cylinder of the same depth. The opacities in polarization 2 are generally larger than for polarization 1, and hence photon density 2 tends to remain trapped longer, becoming optically thin closer to the surface than does polarization 1. The photon densities decrease toward the free surface, where they approach a limiting value. This value is reached at a depth comparable to the mean free path, since the photon densities cannot vary on much shorter depth scales (see Figs. 5–6). While diffusing, photons can change from one polarization to the other, and if they switch to a lower optical depth polarization, they may escape from a deeper layer than if they had remained in their previous polarization. The largest opacity is at the cyclotron frequency (*diamonds*), in particular for polarization 2. The presence of a mixing length (Nagel 1980; Mészáros, Nagel, and Ventura 1980; Bussard and Lamb 1982) is an important feature of polarized radiative transfer. Under the simplifying assumption of coherent scattering, it is meaningful to define the thermalization length as

$$\lambda_m = D_1 D_2 [S_{ex}(D_1 + D_2)]^{-1/2} , \qquad (2)$$

where $D_i = \langle \beta(\theta)/K_i(\theta) \rangle$, $K_i = \alpha_i + \sigma_i$ is absorption plus scat-

tering opacity, $\beta = (\cos^2 \theta, \frac{1}{2} \sin^2 \theta)$ for (slab, column), $\langle \ \rangle$ denotes a suitable angle average, and S_{ex} is the polarization exchange mean opacity, suitably averaged over angles. At depths larger than λ_m, 1 and 2 are closely coupled and have comparable densities, while for depths less than λ_m, they are decoupled and the polarization of lower opacity, which is 1, escapes freely (constant density). The emergent flux is thus given mostly by this polarization 1, while 2 continues slowly diffusing out via $2 \to 2$ scatterings, further decreasing its density until it also becomes optically thin, much closer to the surface. Under the same assumptions, the combined thermalization length can be defined as

$$\lambda_t = \left(\frac{D_1 + D_2}{A_1 + A_2}\right)^{1/2} , \qquad (3)$$

where D_i is as before, and A_i is an angle-averaged absorption coefficient. At depths greater than λ_t, both polarizations are thermal (Wien, in this case, since we have no induced processes). An "effective" thermalization depth is seen in the deep run of Figure 6 (model E), where for all frequencies and polarizations the density saturates to the Wien value and remains constant, for depths greater than an "effective"
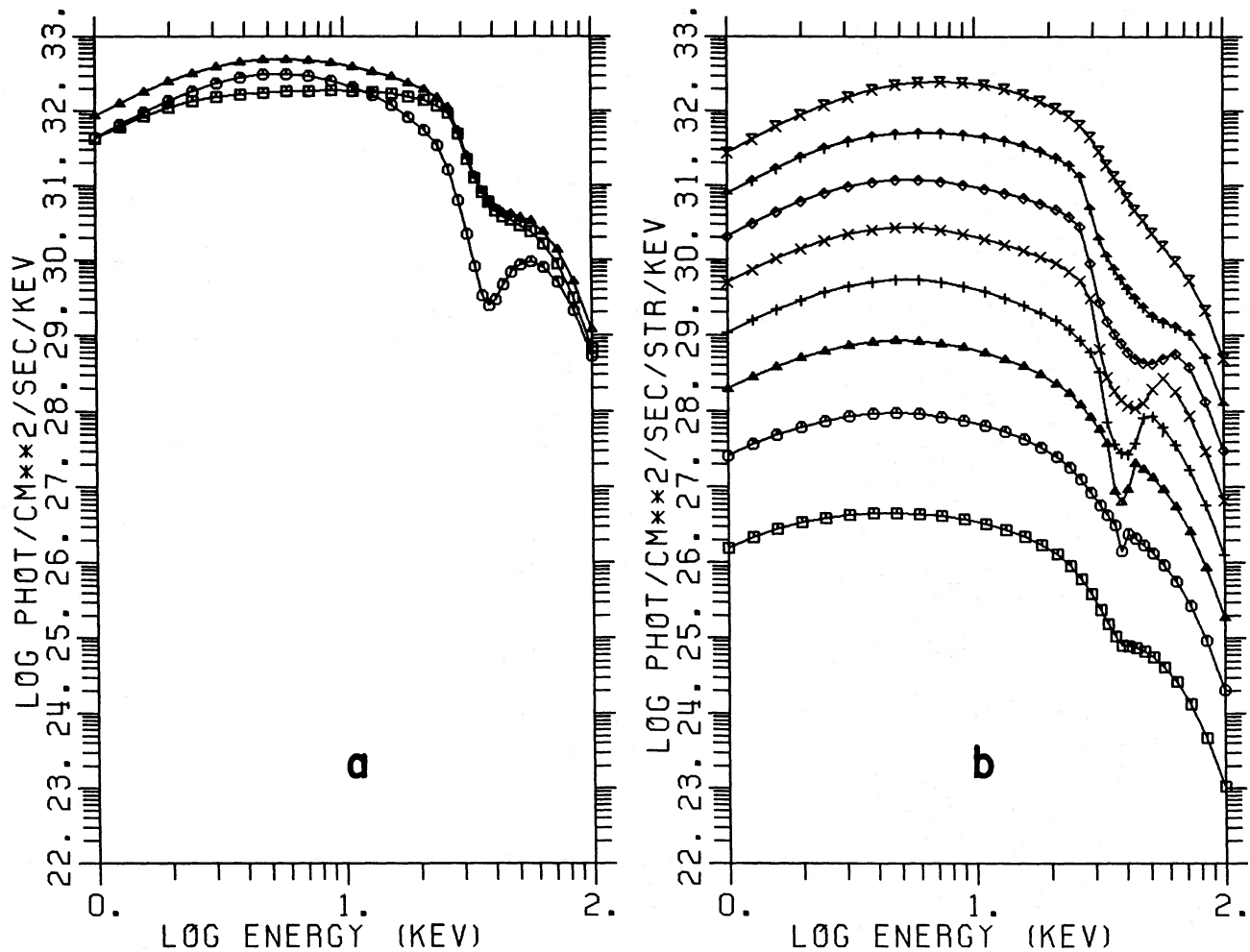
Fig. 3.—Model E, a deep slab of $\rho = 0.5$ g cm^{-3}, $kT = 8$ keV, $\hbar\omega_B = 38$ keV, $R = 10^5$ cm, essentially a semi-infinite atmosphere with B perpendicular to the surface. (a) Flux integrated over angle, symbols as in Fig. 1. (b) Differential flux (1 and 2) for the same eight angles labeled by the same symbols as in Fig. 1. Uppermost curve is 11°, shown at true value, successive lower ones staggered by increasing powers of $10^{-1/2}$.

mixing length. Our choice of $R = 10^5$ cm for these parameters is, therefore, essentially equivalent to a semi-infinite atmosphere. The lower boundary condition of perfect reflection is compatible with this, since in thermal equilibrium the intensity propagating inward should equal that propagating outward. It is important, however, to stress that the mixing and thermalization lengths as defined in equations (2) and (3) are of limited use only, since in the actual incoherent transfer, photons diffuse also in frequency, not just in space. The "effective" thermalization and mixing lengths deduced from Figure 6, which include Comptonization, can be significantly different from the (coherent) expressions (2) and (3), especially for frequencies close to the cyclotron resonance.

IV. BEAM SHAPES AND PULSE PHASE–DEPENDENT FEATURES

We study the directionality of the escaping radiation by plotting in Figures 7 and 8 the flux $F_\omega(\theta) = I_\omega \cos \theta$ (slabs) and $F_\omega(\theta) = I_\omega \sin \theta$ (columns) as a function of angle, these being the beam functions. In Figures 7a and 7b we show the beam functions of the low-depth slab and cylinders, B and C, at the same eight frequencies used in the photon density plots. Again the cyclotron frequency is denoted by the diamonds. Figures 8a and 8b show the beam function for the deep slab and cylin-

der models, E and D. The slabs, Figures 7a and 8a, show the limb-darkening effect. The thin slab is transparent at low frequencies close to the field direction (low angles), causing a low-frequency darkening near the normal to the slab (Fig. 7a, square, circle, and triangle at small angles). At higher frequencies, including the cyclotron resonance (diamonds), the flux is maximum near the normal and drops off towards high θ. However, on the wings of the resonance (the frequencies above and below resonance), the maximum occurs at intermediate angles. This is caused by the strong angular dependence of the cyclotron line shape. Since close to 90° the line becomes very sharp, for frequencies above or below the resonance the plasma is actually more transparent at large angles than at small angles. Thus photons will escape preferentially in these directions. The deep slab, Figure 8a, shows the same behavior at high frequencies and near the resonance, but due to its very large optical depth, it is never transparent, even close to the magnetic field direction. Thus, the darkening at low frequencies and low angles is not seen in the deep slab.

The low-depth and deep cylinder are seen in Figures 7b and 8b. The limb darkening, here given by a sin θ factor, occurs now at low angles (surface normal is now at $\theta = 90°$). The behavior is fairly regular. The most distinctive feature is the
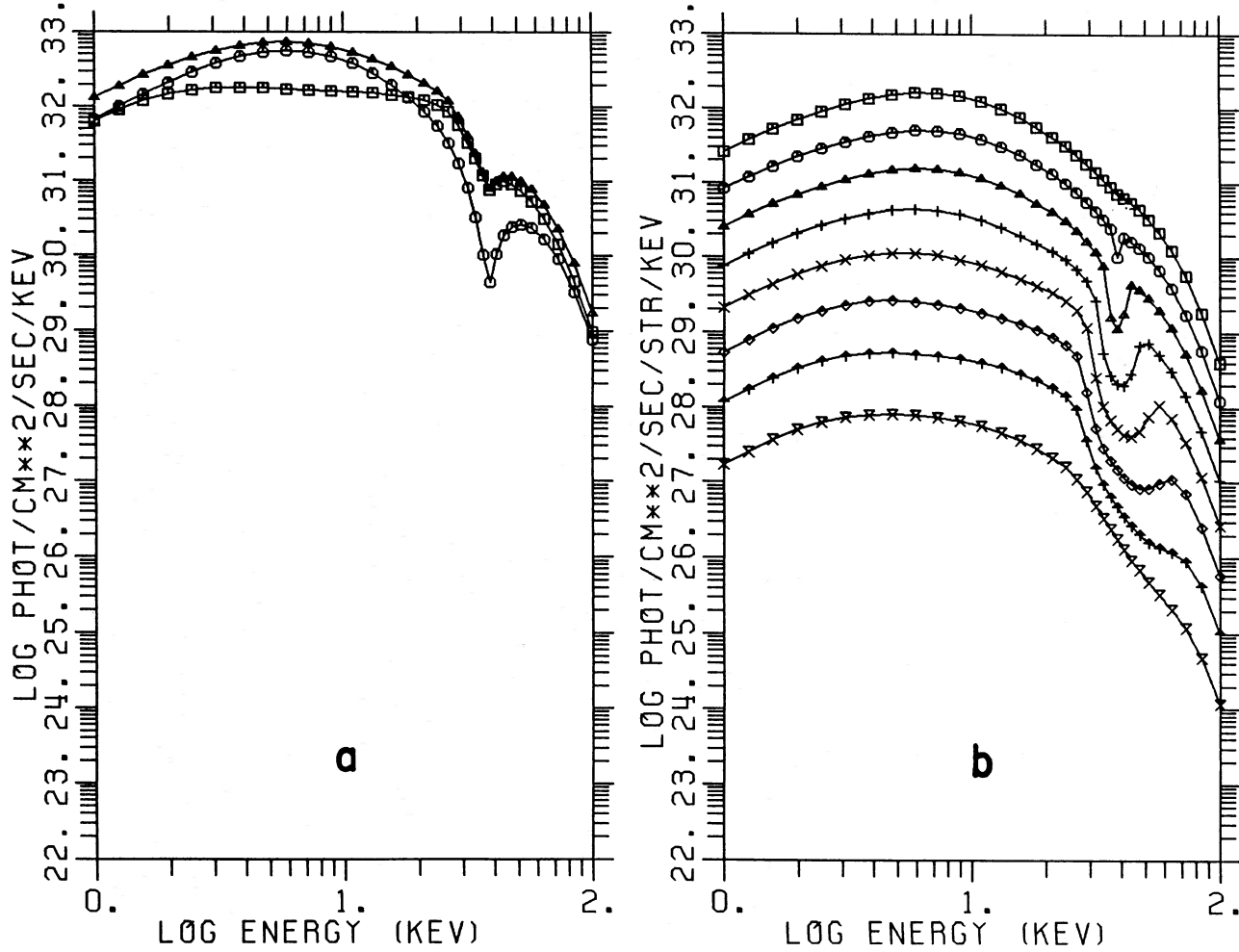
FIG. 4.—Model D, a deep column of $\rho = 0.5$ g cm^{-3}, $kT = 8$ keV, $\hbar\omega_B = 38$ keV, $R = 10^5$ cm. This is essentially a semi-infinite atmosphere with B parallel to the surface. (a) Flux integrated over angle, symbols as in Fig. 1. (b) Differential flux (1 and 2) for the same eight angles as in Fig. 1, uppermost being 89°.

very pronouned increase in the flux close to 90° at the cyclotron resonance, where the cross section peaks strongly in the transverse direction. The wings, at high angles, again are enriched with photons scattered out of the resonance.

The fact that the radiation is beamed, with a well-defined directionality pattern with respect to the magnetic field direction, gives rise to the pulses seen by an observer as the neutron star rotates. Calling i_1 the angle between the rotation axis and the line of sight, and i_2 the angle between the magnetic field and the rotation axis, the phase ϕ is related to the direction θ between the line of sight and the magnetic field (which is also the angle of the wave vector with respect to B) through the expression

$$\cos \theta = \cos i_1 \cos i_2 + \sin i_1 \sin i_2 \cos 2\pi\phi . \qquad (4)$$

The extreme values of θ observable from a particular object are $|i_1 - i_2|$ at $\phi = 0$, and $i_1 + i_2$ at $\phi = 0.5$. For a slab, the main pulse comes at $\phi = 0$ (or 1), while for a cylinder it comes at $\phi = 0.5$. When $i_1 + i_2 > 90°$, at some phases one sees the "other" pole as well, seen at $\theta' = 180° - \theta$, giving rise to the interpulse at $\phi = 0.5$ (slab) or at $\phi = 0$ (cylinder). We show the pulse shapes for 5 different sets of viewing angles, $(i_1, i_2) = (50°, 20°)$, $(45°, 45°)$, $(75°, 45°)$, $(60°, 45°)$, and $(80°, 60°)$ in that order

from left to right. Note that i_1 and i_2 are interchangeable in expression (4). The pulses are shown for the eight frequencies selected before, from bottom to top. The sixth curve up is the cyclotron frequency. Figures 9a and 10a show the normalized pulse shapes for the low-depth and deep slabs. There are slight differences, e.g., for (45°, 45°) the second curve up is split in the thin case but full in the deep case, as expected. A very interesting fact emerging from these calculations is that the pulses are narrowest (lowest duty cycle) at the resonance, consonant with the fact that the radiation is most strongly beamed (asymmetric) at the resonance. Thus, the normalized pulses are sharpest and narrowest at the resonance. In the wings, at frequencies just below and above the resonance, the secondary peak at intermediate angles, indicated in the beam discussion, is responsible for the appearance of a triple peak structure. At some viewing angles, the side peaks are even stronger than the central peak, giving the appearance of an apparent pulse inversion in the wings. This new phenomenon is caused primarily by the inclusion of Comptonization in our calculation and has not been discussed before. This is not to be confused with the splitting up of pulses, at frequencies well below the resonance, into double or multiple pulses, which is predicted also by strictly coherent calculations for shallow depths (Basko and
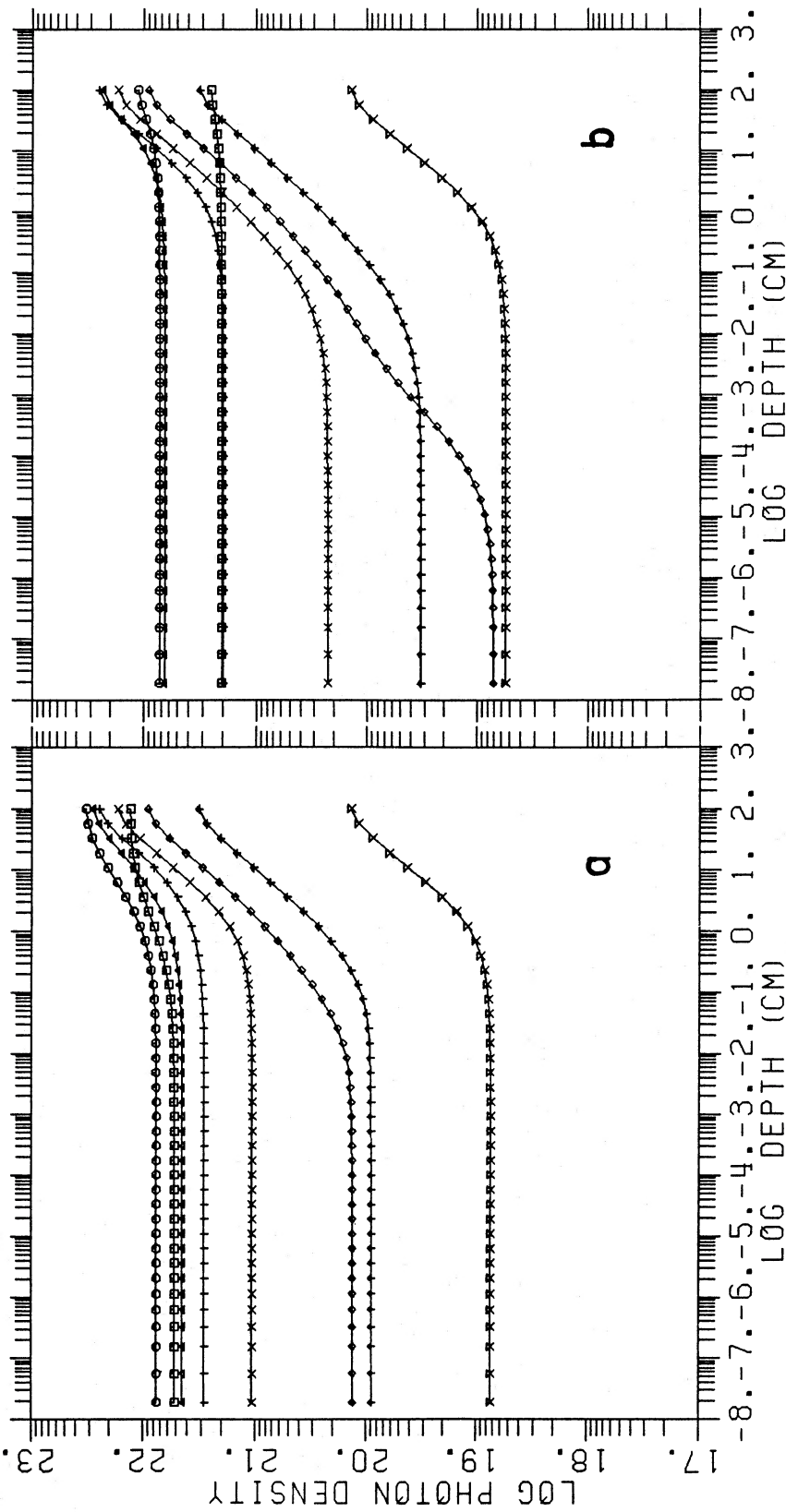
FIG. 5.—Photon density (photons cm^{-3} keV^{-1}), shallow slab (B) of Fig. 1, as a function of spatial depth, for the frequencies 1.6, 3.8, 9.0, 18.4, 29.1, 38.4, 51.7 and 84.7 keV (squares, circles, triangles, plusses, crosses, diamonds [cyclotron frequency], arrows, and closed crosses respectively); (a) Polarization 1, (b) Polarization 2.

144
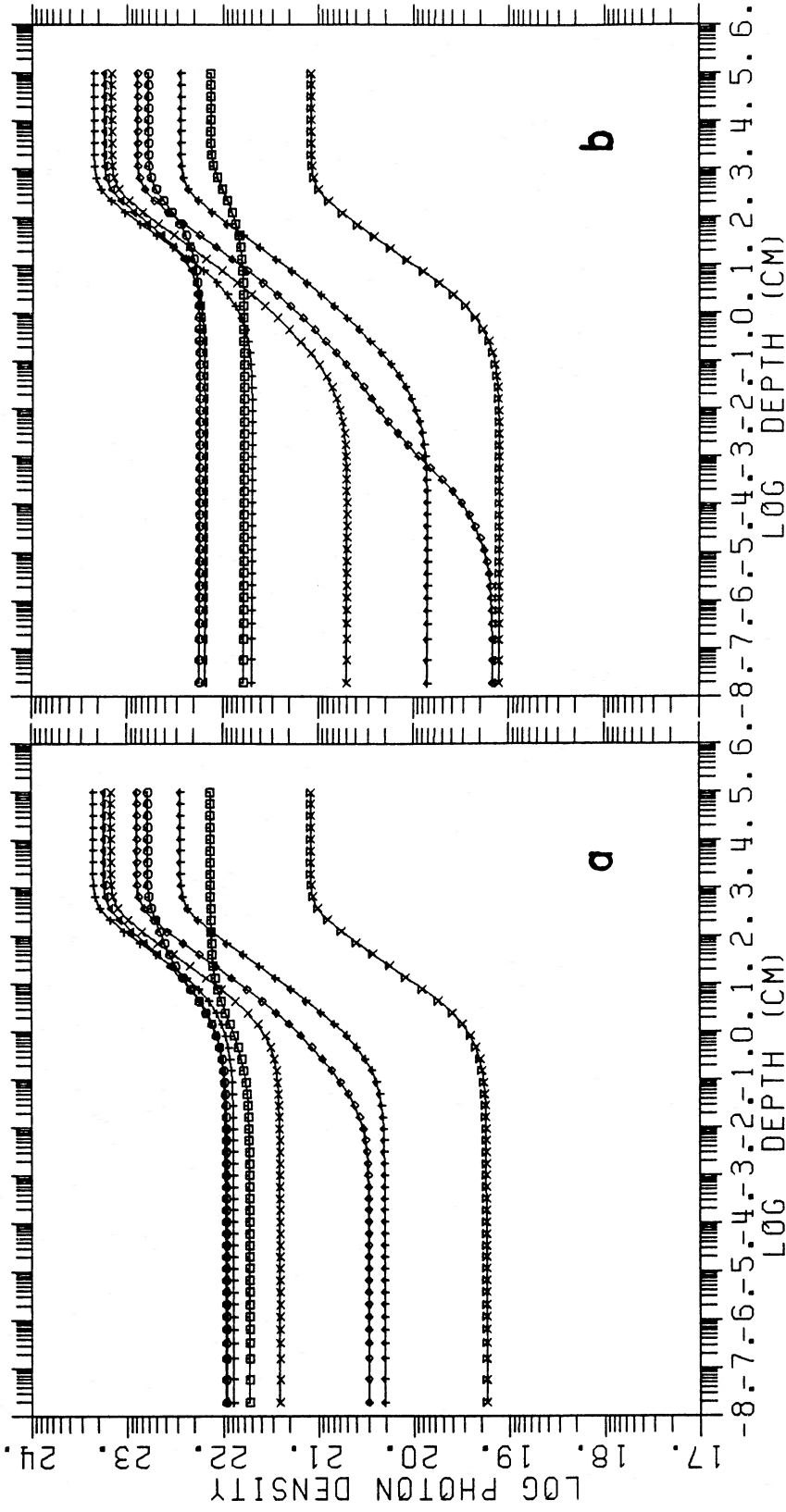
Fig. 6.—Photon density for the deep slab (E) of Fig. 3, same symbols as in Fig. 5; (*a*) Polarization 1, (*b*) Polarization 2

145
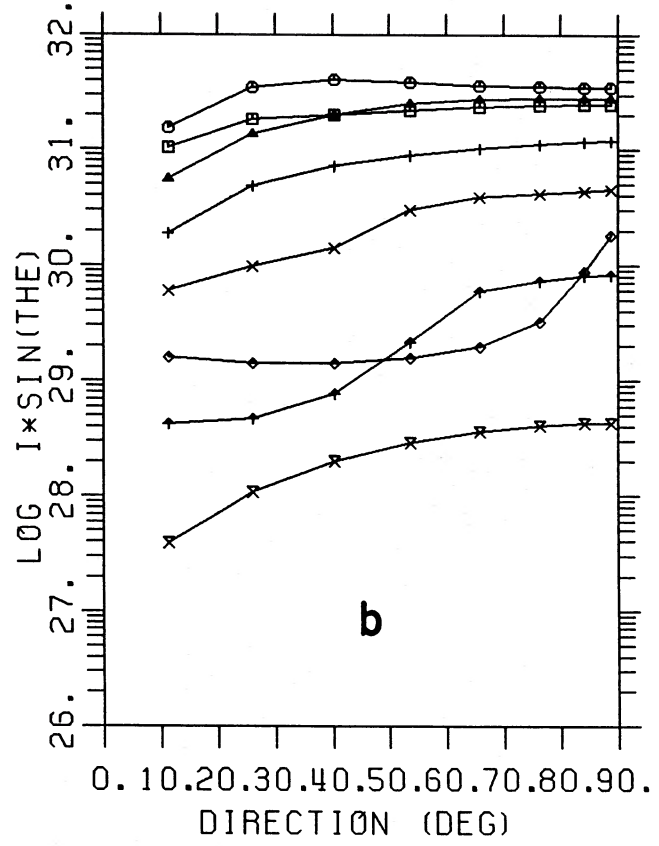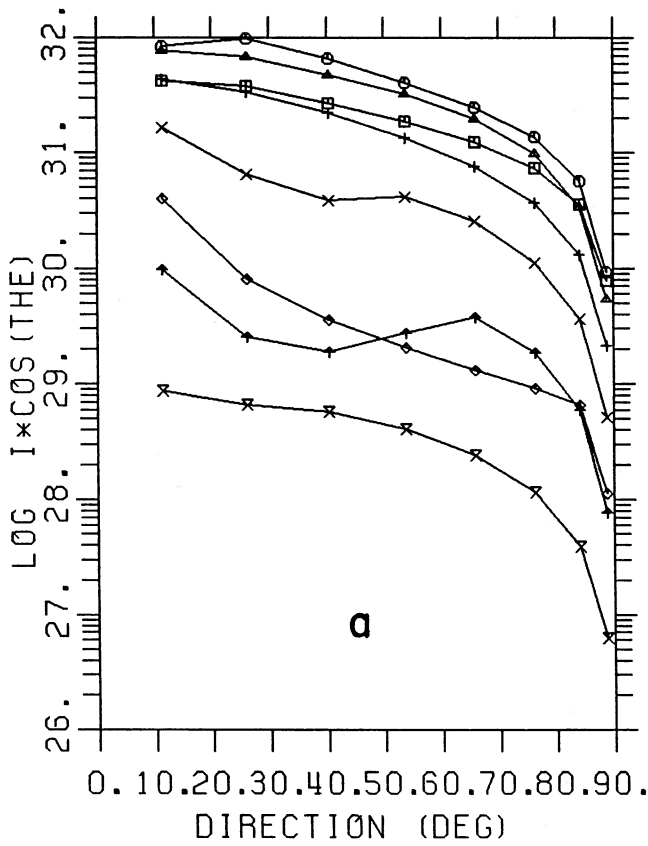
Fig. 7.—Beam function (1 and 2) for the shallow slab (B) of Fig. 1, $I_\omega(\theta)$ cos θ, and the shallow column (C) of Fig. 2, $I_\omega(\theta)$ sin θ, plotted as a function of angle for the same frequencies as in Fig. 5; (a) Shallow slab (B), (b) Shallow slab (C).
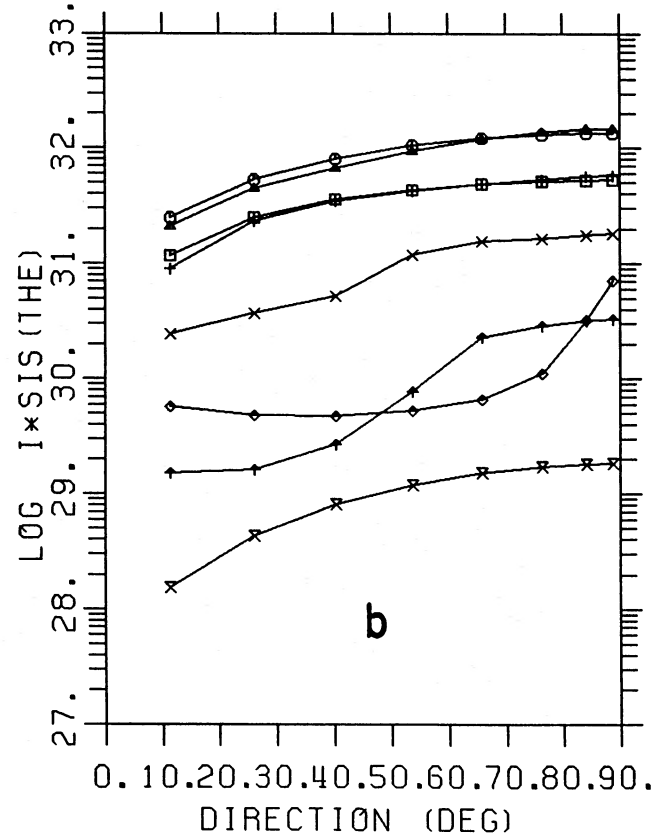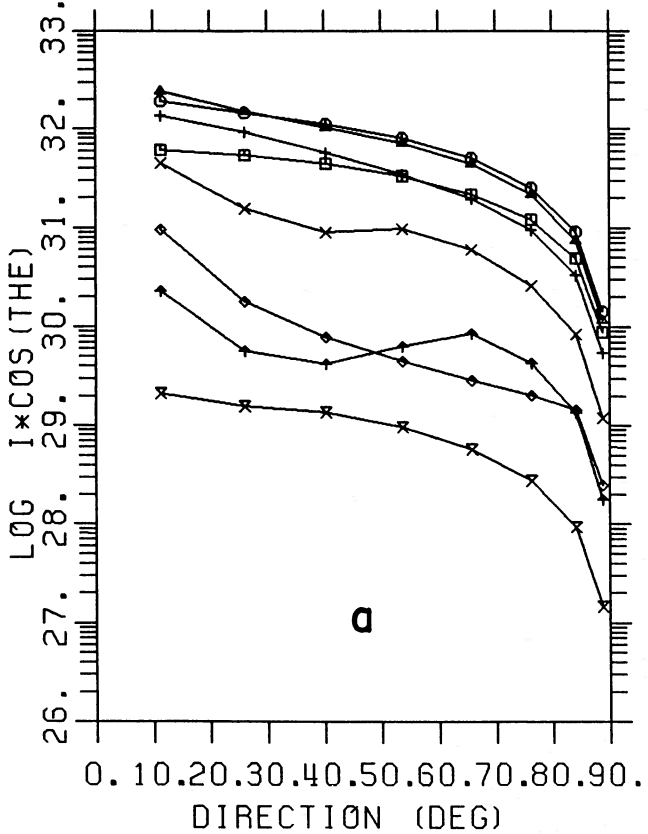
Fig. 8.—Beam function (1 and 2) for the deep slab (E) of Fig. 3, $I_\omega(\theta)$ cos θ, and the deep column (D) of Fig. 4, $I_\omega(\theta)$ sin θ, same symbols as in Fig. 7; (a) Deep slab (E), (b) Deep column (D).

146
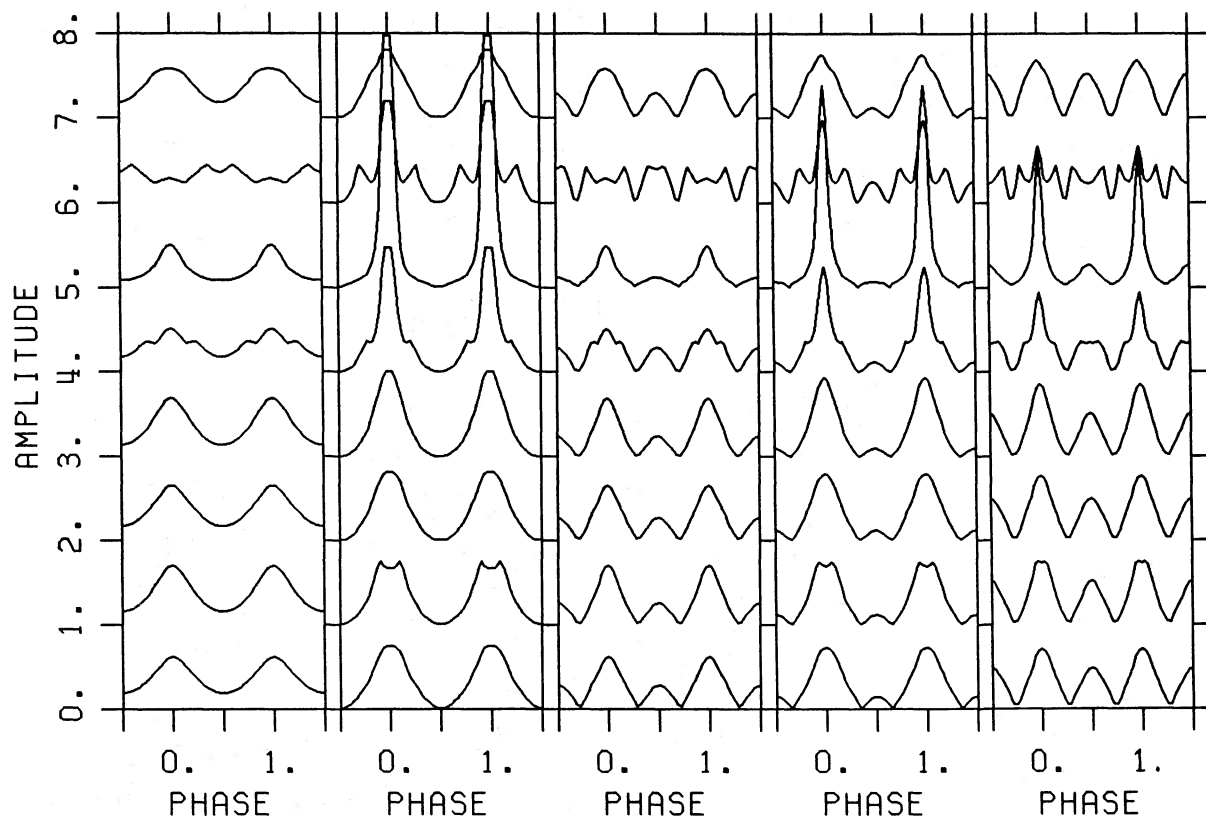
FIG. 9a
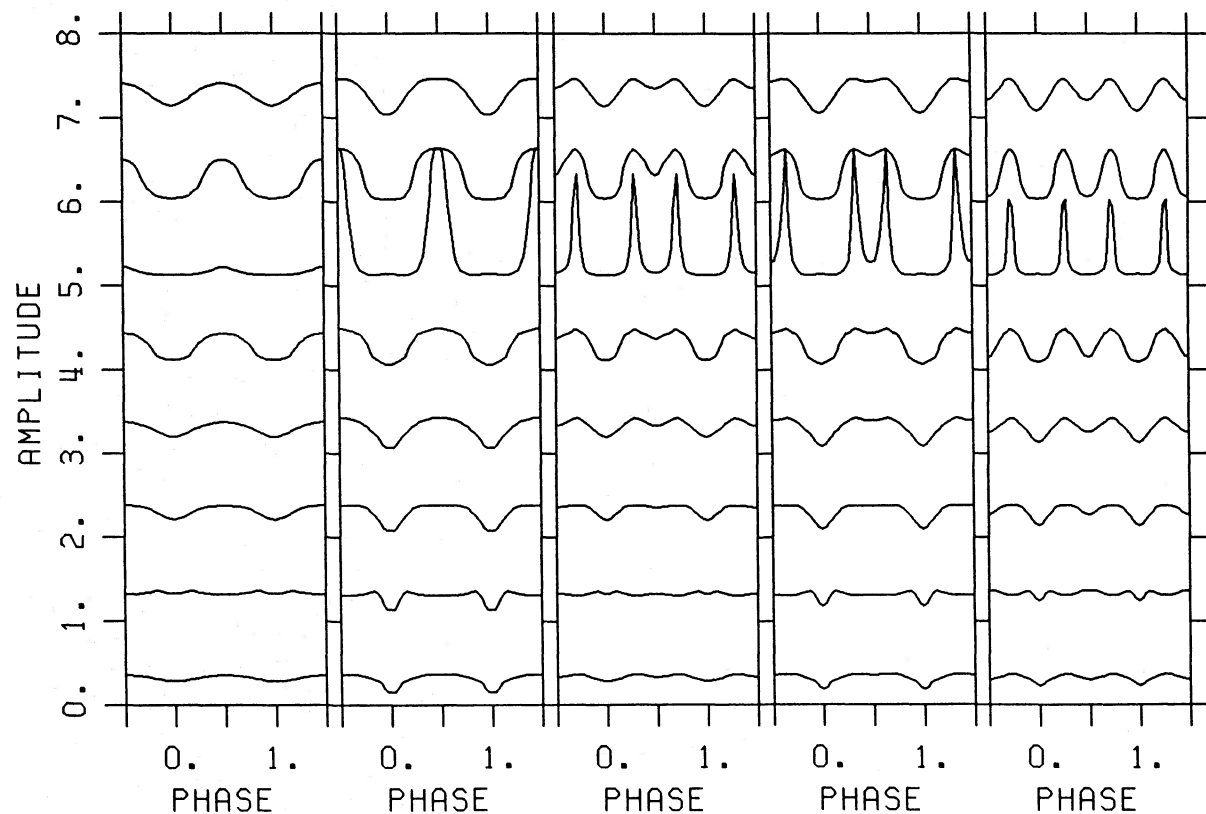
FIG. 9b

FIG. 9.—Normalized pulse shapes (1 and 2) for the viewing angles (i_1/i_2) having values from left to right (50°/20°), (45°/45°), (75°/45°), (60°/45°), and (80°/60°), where i_1 is interchangeable with i_2. Pulses are shown for the frequencies 1.6, 3.8, 9.0, 18.4, 29.1, 38.6, 51.7 and 84.7 keV (*bottom to top*). The cyclotron frequency is the third curve down from the top. (*a*) Shallow slab (B) of Figs. 1, 5, and 7*a*; (b) Shallow column (C) of Figs. 2, 6, and 7*b*.

147
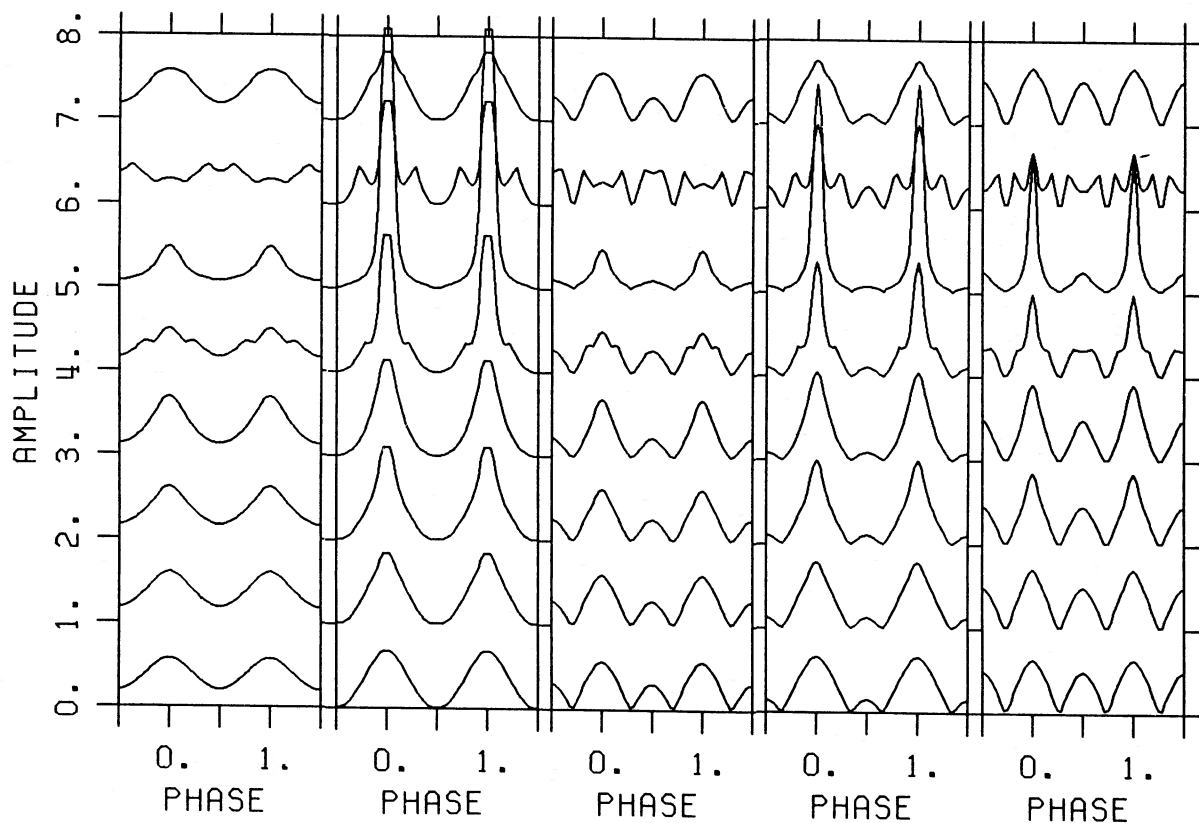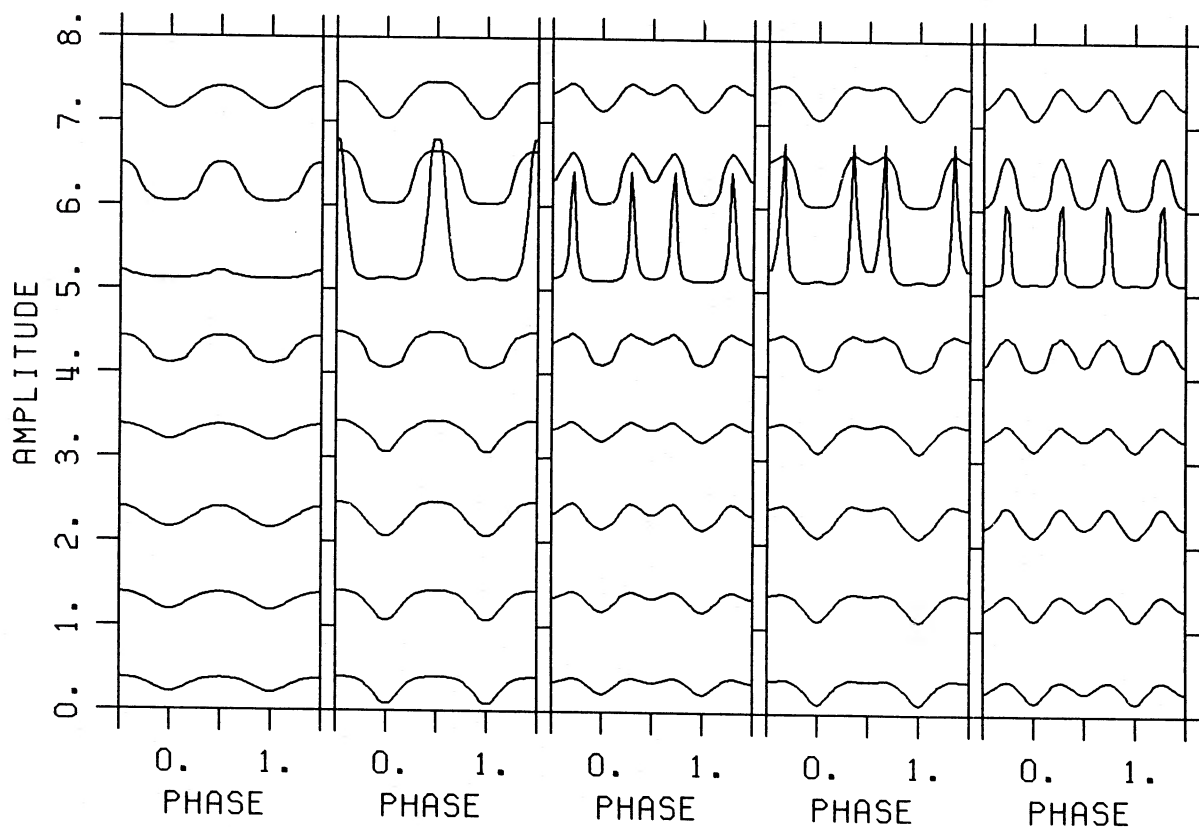
FIG. 10a

FIG. 10b

FIG. 10.—Normalized pulse shapes (1 and 2), as in Fig. 9. (a) Deep slab (E) of Figs. 3 and 8a; (b) Deep column (D) of Figs. 4 and 8b.

Sunyaev 1975; Kanno 1980; Nagel 1981a; Mészáros and Bonazzola 1981). This effect is also seen in our incoherent scattering calculations here, e.g., in Figure 9a for (45°, 45°).

The pulse shapes for the low-depth and deep cylinders (Figs. 9b and 10b) are shown for the same five sets of viewing angles. Inspection of them confirms Nagel's result (1981a) indicating that cylinders produce much broader pulses than do the slabs. The beam shape is, however, more strongly beamed at the resonance in the column case. This translates into very sharp peaks at the resonance, for a fraction of the possible viewing angles (those that sample the direction close to $\theta \approx 90°$). But at (50°, 20°) of Figure 9b, which does not reach that far, the pulse at the resonance is even more featureless than at other frequencies. When $\theta \approx 90°$ is sampled, as in the last three sets of viewing angles, extremely narrow *double* peaks appear at the resonance. This is in fact a very interesting new result, since it would allow one to discriminate between slab and cylinder models, the former being single-pulsed at the resonance, and the latter being double (unless the viewing angles conspire against this).

V. EXTERNAL ILLUMINATION

We consider now a low-density slab model (F), characterized by $kT = 7$ keV, $\hbar\omega_B = 38$ keV, and $\rho = 1.67 \times 10^{-4}$ g cm^{-3}, which besides its own thermal emission and absorption also has an external illumination at the outer boundary $r = R$. This external source is assumed to produce seed soft photons with a blackbody spectrum at $T_{bb} = 0.1$ keV, but 10^4 times more numerous than for a thermal source at that temperature. The depth of the atmosphere is taken to be $y = 16.7$ g cm^{-2}, or $R = 10^5$ cm at this density. The results for illumination from the lower boundary are essentially the same as for illumination from the outer boundary (Paper I), so that we need not treat that case separately. A reflecting inner boundary is adopted. As discussed in Paper I, a free-streaming inner boundary would produce the same hard X-ray spectrum at the outer boundary ($r = R$) as an atmosphere of half the previous height, $R' = R/2$, and a reflecting inner boundary. Figure 11a shows the angle-integrated total and polarized fluxes from such a slab. The main difference, as compared to self-emitting models B, C, E, and D is that this model (F) has a total photon number slope of about -1 in the 2–20 keV range. Since the photons are not thermal, there is no low-energy thermal turnover below $kT = 7$ keV, the temperature of the slab. In Figure 11b we show the total differential fluxes $I_\omega(\theta) \cos \theta$ for the same set of eight angles. The soft flux $\hbar\omega < 1$ keV is not shown in Figure 11, having already been discussed in Paper I. The soft flux is dependent on the boundary conditions (reflection or
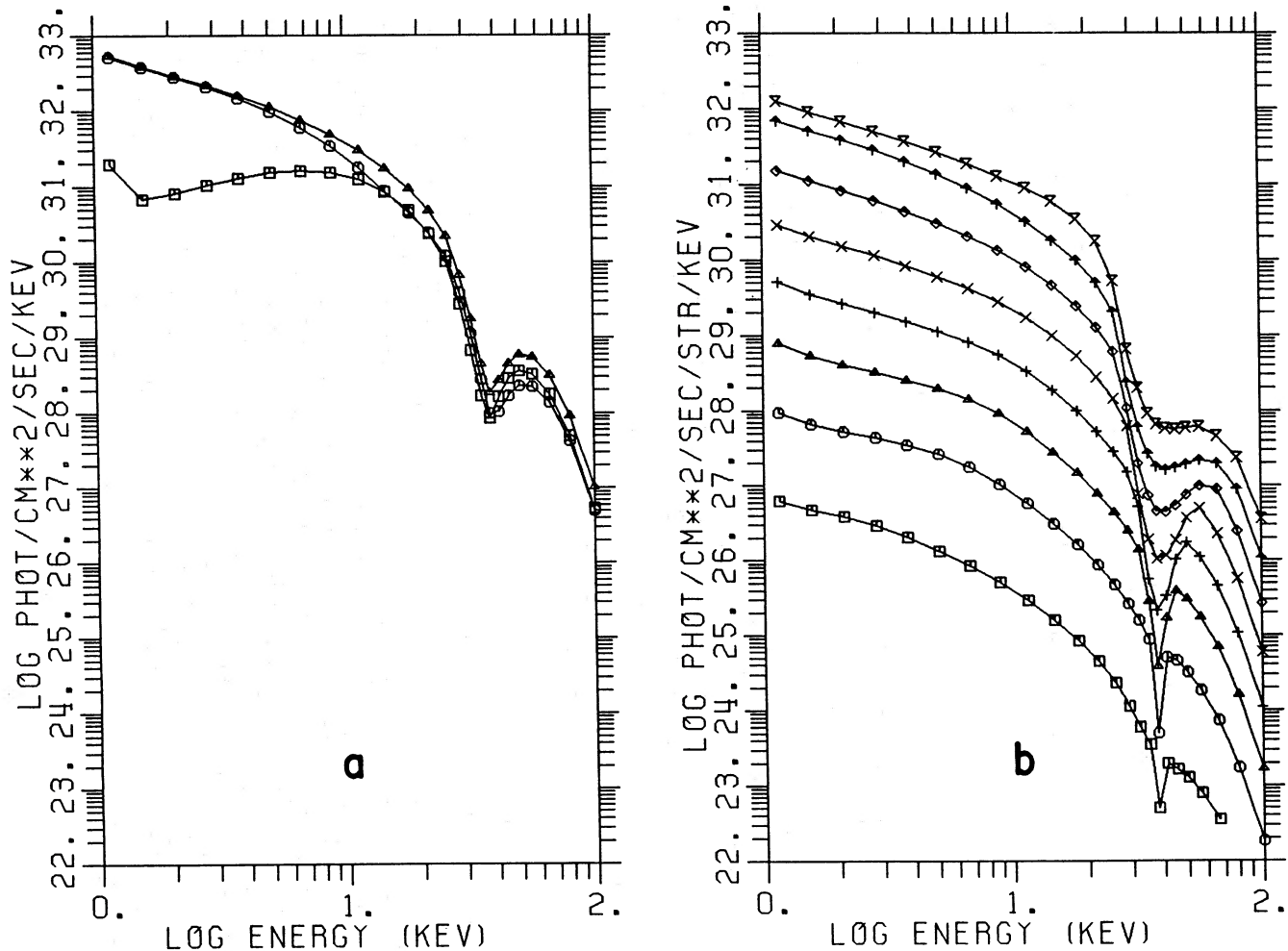
FIG. 11.—Model (F), a slab illuminated by an external source of soft ($E_s < 1$ keV) photons. The slab has $\rho = 1.67 \times 10^{-4}$ g cm^{-3}, $kT = 7$ keV, $\hbar\omega_B = 38$ keV, $R = 10^5$ cm, and magnetic field perpendicular to the surface. (a) Flux integrated over angle. *Squares*, polarization 1; *circles*, polarization 2; *triangles*, 1 plus 2. (b) Differential flux $I_\omega(\theta) \cos \theta$ for the same eight angles labeled by the same symbols as in Fig. 1.
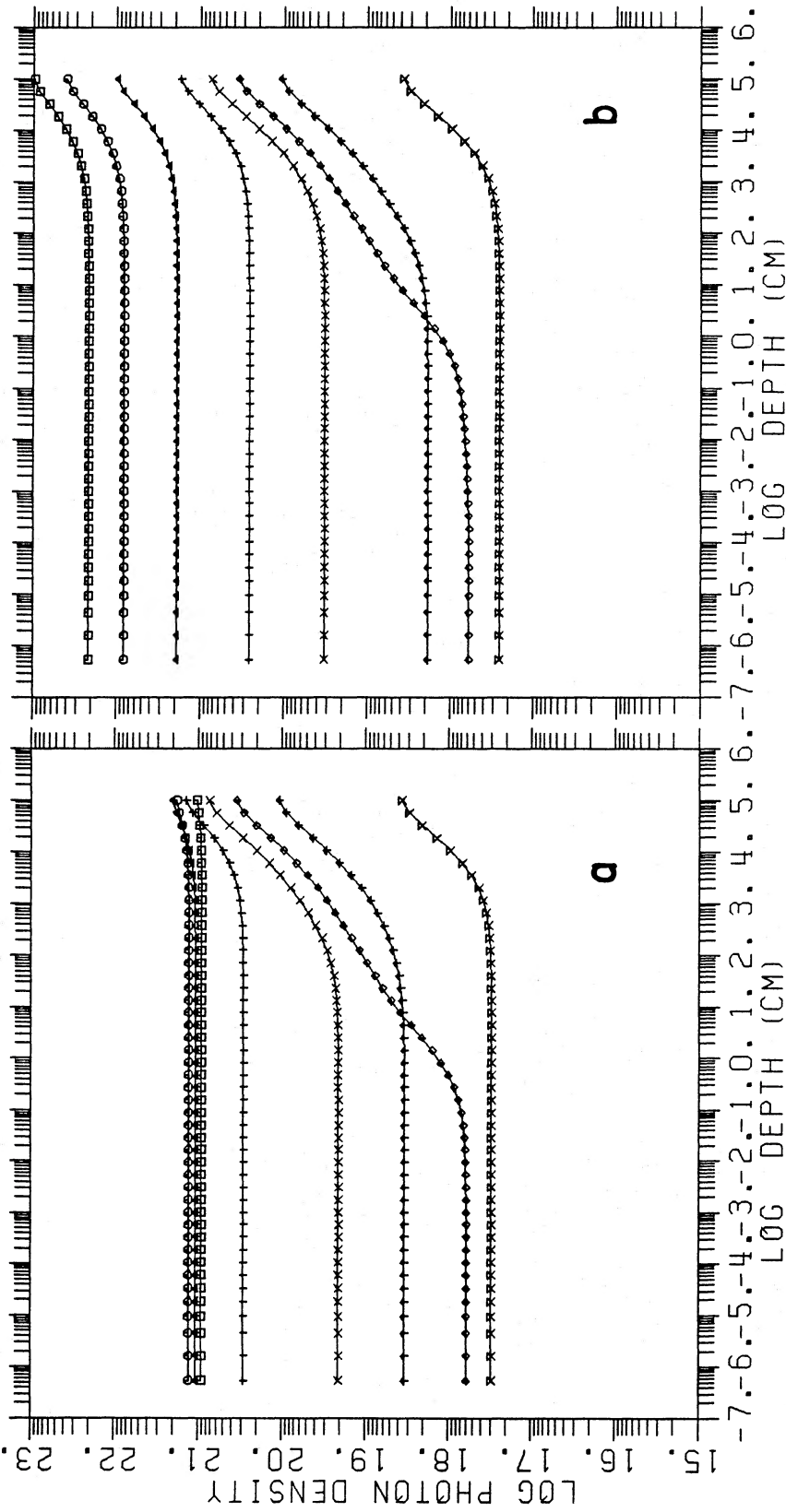
Fig. 12.—Photon density of model (F), slab illuminated by an external soft source. For the frequencies 1.6, 3.8, 8.9, 18.3, 29.1, 38.4, 50.2, 80.2 keV (squares, circles, triangles, plusses, crosses, diamonds [cyclotron frequency], arrows, and closed crosses respectively). (a) Polarization 1; (b) Polarization 2.

transmission) and the intrinsic details of the soft source, which we ignore. However, the hard-X-ray flux consists of photons that have been scattered many times, and therefore this is more model-independent. As for the other slabs, the 11° angle (*closed cross*) differential flux in Figure 11*b* shows the actual value, 26° (*arrow*) is actual times $10^{-1/2}$, 40° (*diamond*) is actual times 10^{-1}, etc. This exaggerates the limb-darkening effect. Whereas in the self-emitting atmospheres this renormalization did not change the actual ordering of the curves, here in model F it obscures the fact that $F(11°)$ is actually *lower* than $F(26°)$, and $F(26°) \approx F(40°)$, while subsequent fluxes behave with the usual slab monotonicity (decreasing flux with increasing angle). This qualitative difference from the self-emitting slabs is caused by the much lower optical depth of this model F. The total opacity at frequencies below ω_B, furthermore, decreases as a function of decreasing angle and decreasing frequency (approximately as $[\omega/\omega_B]^2$ and $\sin^2 \theta$, see Börner and Mészáros 1979). In this low-opacity model, fed by low-frequency photons, there is thus a relative lack of hard photons at angles close to the magnetic field direction, as compared to high-optical depth thermal models. Another difference is that the cyclotron feature is more pronounced at all angles, since thermal emission at ω_B cannot replenish the photons scattered out of the resonance. The photon density of model F as a function of depth is shown in Figure 12. One can see in Figure 12*a* the low opacity in the ordinary mode at low frequencies, where photons can almost stream out freely, while in the extraordinary polarization or at higher frequencies the higher optical depth enforces the usual diffusive behavior.

The beam function at different frequencies as a function of angle, $F_\omega(\theta) = I_\omega(\theta) \cos \theta$, is shown in Figure 13 for model F. The distinguishing feature of the low optical depth is the lack of photons at low angles (e.g., Basko and Sunyaev 1975, and others), i.e., the presence of a "hole" in the center of the pencil beam pattern, at frequencies below the resonance. Note that the higher optical depth models show this only at the lowest frequencies. On the other hand, our model F shows that such a hole is *not* present at the cyclotron frequency, and this holds also for B, C, E, and D. The hole is explained as being due to a reduced opacity at low angles, but at the cyclotron frequency the resonance increases it, and one obtains (qualitatively) the usual limb-darkening behavior. The shoulders at intermediate angles on both wings of the resonance, discussed in § IV, are also seen here.

The pulse shapes for model F are shown in Figure 14 for the same viewing angles as before. The effect of the hole in the beam is clearly seen at viewing angles which sample close to $\theta \approx 0°$, e.g., in the second, fourth, and fifth sets of viewing angles, producing a double-peaked main pulse at most frequencies except near the resonance. Other viewing angles, e.g., the first and third, mostly avoid the hole and give single pulses at all but the highest frequencies. Note that for higher optical depth models B, C, E, and D, even the viewing angles which sampled close to $\theta \approx 0°$ resulted in single pulses, because there are more scatterings and therefore an increased probability of scattering into the low-angle region.

VI. DISCUSSION

The angle-dependent incoherent scattering calculations using eight angles × 32 frequencies extend our more limited investigation of Paper I. The cyclotron line profile is here well resolved over five to six angles but remains unresolved at angles larger than ~80°. In any case, the frequency resolution
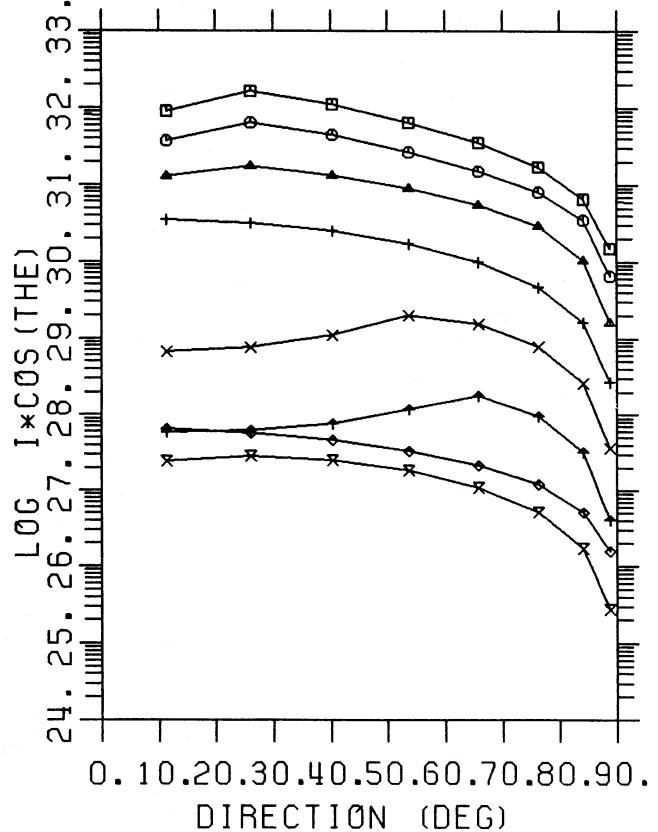
FIG. 13.—Beam function $I_\omega(\theta) \cos \theta$, (1 and 2), for model (F), same frequencies and symbols as in Fig. 12.

near the resonance is $\Delta\omega/\omega_B \approx 2.5/38 = 0.07$, which is better than most observational capabilities. A different choice of angular grid could give more information at the lower angles but would decrease the numerical accuracy, unless one introduces other techniques. The effect of doubling the number of angles, from four to eight, does not modify significantly the total (angle-integrated) spectrum. However, the transition from one angle (cf. Nagel 1981*b*) to four or more angles (Papers I and the present work) does introduce some changes, in the sense that with only one angle (60°), the spectra are somewhat harder than if more angles (≥ 4) are included. As discussed in Paper I, this is related to the lower opacity, and therefore easier photon escape at low angles, such as $\lesssim 21°$. The main advantage of using eight angles is that it is the minimum needed to obtain a reasonably detailed description of the pulse shapes. The effect of Comptonization on the beam and pulse shapes does not introduce significant differences with respect to previous coherent-scattering calculations (e.g., Nagel 1981*a*; Kaminker, Pavlov, and Shibanov 1982; Harding *et al.* 1984), provided we look at frequencies $\omega \lesssim 0.5\omega_B$. For larger frequencies, the present incoherent-scattering pulse and beam shapes depart noticeably from coherent ones, especially near the resonance, as expected. In this latter frequency range, errors introduced by assuming a homogeneous plasma are probably less significant than those which would be introduced by leaving out incoherent scattering effects.

The effect of vacuum polarization, in addition to Doppler and recoil effects in the scattering, is very important in determining the structure of the cyclotron line, in particular its
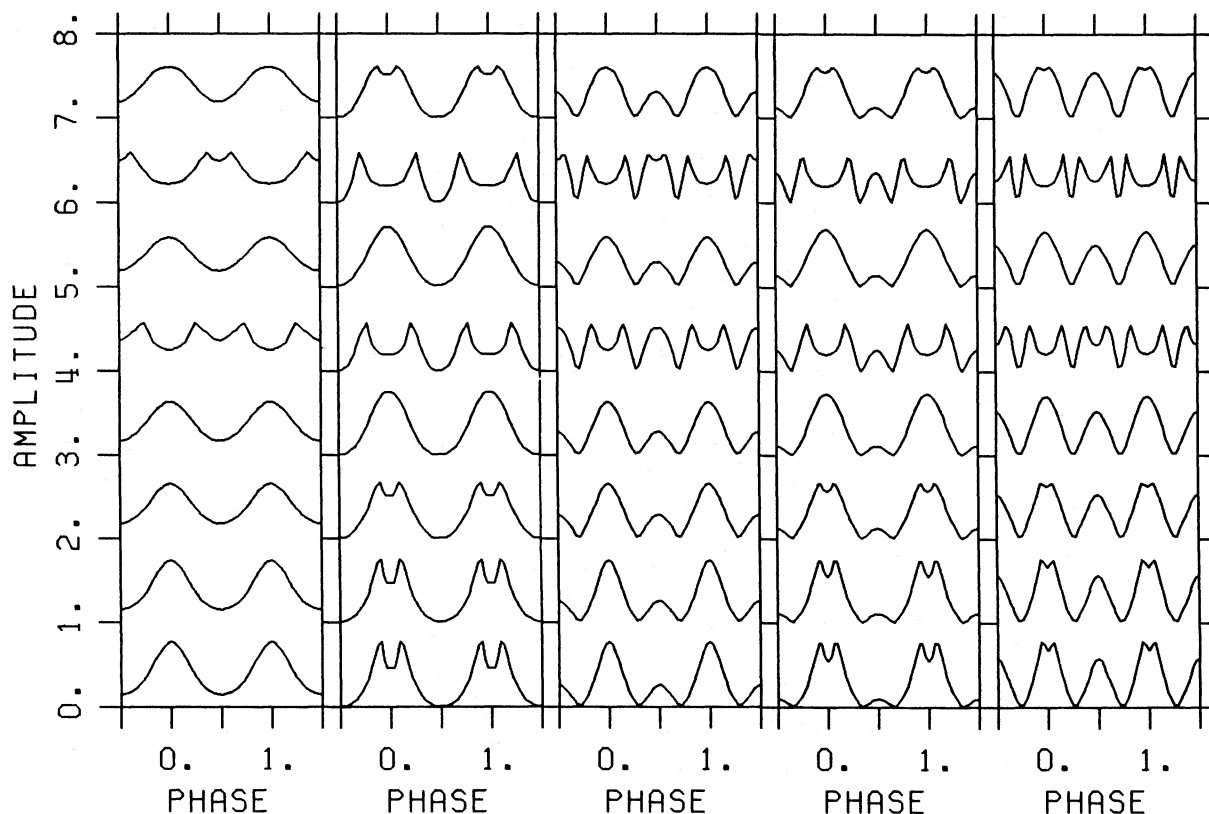
FIG. 14.—Normalized pulse shapes (1 and 2) for model (F), slab with external soft external illumination. The same five viewing angles as in Fig. 9 are shown left to right, and the same eight frequencies as in Fig. 12 are plotted from bottom to top. The cyclotron frequency is the third down from the top.

depth and shape. An "approximate" inclusion of vacuum effects is sometimes done by using the usual cross sections with linearly polarized modes, on the grounds that the vacuum imposes "almost" linearly polarized modes. This approximation can be dangerous, since the polarization is vacuum-dominated only between $\omega_{v1} \approx 3(n_e/10^{22})^{1/2}(B/4.4 \times 10^{12})^{-1}$ keV and $\omega_{v2} \approx \omega_B$, and for $n_e \lesssim 10^{24}$ cm^{-3}. For $\omega \leq \omega_{v1}$ or $\omega \geq \omega_B$, the polarization is plasma-dominated. Thus a study of the line profile itself must of necessity include both plasma *and* vacuum effects.

A general distinction between slab and column models is that, for slabs, the cyclotron trough (and the blue wing shoulder) appear at higher energies with increasing angle away from the normal, whereas for columns this behavior is reversed. This behavior is clearly seen in Figures 1b and 2b, as well as others. It is basically due to the Doppler shift of the resonance as seen by an electron moving along the field. As discussed in Paper I, where some use was made of advance results from our present eight-angle calculations, a comparison of the calculated line blue wing shift with the observations of Voges et al. (1982) favors a slab model, and this is confirmed here.

Another general distinction between slab and column models can be seen by examining Figures 9a and 9b, or 10a and 10b. The slabs at energies below the resonance give a stronger modulation and a duty cycle compatible with typical observed pulses (e.g., White, Swank, and Holt 1983), while columns give rather weaker modulation and far broader peaks. On the basis of coherent scattering calculations at frequencies below about $\omega_B/2$, Nagel (1981b) reached a similar conclusion.

On the basis of our current calculations, we can here, in addition, discuss the pulse behavior at and above the line as well. Looking at Figures 9 and 10, it is evident that at the resonance, the modulation is maximal. This is seen for a large range of viewing angles, with some exceptions such as (50°, 20°, *leftmost*) in Figures 9 and 10, which does not sample close enough to the surface normal. This increased modulation at the resonance, for viewing angles sampling the normal, is seen in both slabs and columns, but more strongly in the latter. For the last three viewing angles, the column main pulse at the resonance is not only extremely sharp, but it is also split (double). This can be taken as a test for column-like models: at most viewing angles, a sharply split main pulse should appear at the resonance but not above or below it. In Her X-1, the pulse at resonance is single, e.g., Voges et al. (1982). Coupled with the duty-cycle fit at subcyclotron energies, this is a strong argument in favor of a slab model for Her X-1.

An observational feature noted by White, Swank, and Holt (1983) in GX 1+4, 4U 1626−27, and possibly some other X-ray pulsars is a phase reversal of the pulses by 180° in the medium X-ray range. A pulse minimum (trough) at high energies is replaced, at lower energies, by a maximum with a central depression, or notch, accompanied by a general softening of the power-law spectral index. At lower energies still, in 4U 1626−67, the trough reappears again, and the power law becomes harder. This behavior *could* be reproduced by the slab model F (Fig. 14) at (50°, 20°) viewing angles (*leftmost*). At the highest energies the trough is at phase 0.5, and the same is true at energies less than about $\hbar\omega_B/2$ (*lowest four curves*). However, in the energy band $0.5\omega_B \lesssim \omega \lesssim 1.5\omega_B$, there is a peak with a

central notch at phase 0.5. At the resonance itself, there is a trough again, but this has lower intensity than the wings, so that it would not contribute much when integrating over a wide band as White *et al.* do. In addition, the power law index between 5 and 20 keV of model F (in Fig. 11*b*) is seen to be smallest (hardest) at the angles closest to the normal (*upper curves*), i.e., at the hard pulse maximum (phase 0 or 1 here), but the index is larger (softest) at angles farthest from the normal, at the hard pulse minimum, or phase 0.5 here. This is in qualitative agreement with the observations as reported in the reference above. Other slab models, e.g. B of Figure 9*a*, could possibly fit, but neither of the two columns C or D seems to work in this sense (they do not show anything resembling a phase reversal with energy). White, Swank, and Holt (1983) have suggested as an explanation of the phase inversion in GX 1+4 and 4U 1626−67 a transition from pencil beam to fan beam emission. Here we suggest the alternative explanation, that the phase inversion occurs in the neighborhood of the cyclotron frequency. In GX 1+4, the inversion comes in the lowest energy band, and averaged over phase the spectrum looks featureless. If our hypothesis is correct, our calculations may not apply directly to this source, since several harmonics would be involved, and the features could get washed out for $kT \gg \hbar\omega_B$. In 4U 1626−67, a depression followed by a shoulder at higher energies is visible in the hard pulse spectrum shown by White *et al.*, and this *may* be a cyclotron feature. However, a proper testing of the data would be necessary under this hypothesis, in order to be sure.

The models discussed here are of course very simplified, to be manageable. The conclusions to be drawn from them are necessarily tentative. Some problems of interpretation remain. For instance, for Her X-1, the phase-averaged spectrum of model F, a moderate-depth slab illuminated externally by soft photons, fits the spectrum fairly well, as discussed in Paper I. The pulse profiles predicted from model F in Figure 14 indicate a split pulse just above and below the resonance and single at other frequencies, becoming possibly double again at low frequencies. The pulse shapes of Voges *et al.* (1982) do not show a definite splitting above and below the resonance (although the top flattens, and there is perhaps a hint of splitting). Whether such discrepancies can disappear by a proper adjustment of model parameters or by rebinning of the data remains to be seen. Some caution clearly is indicated.

To recapitulate, on the basis of the models discussed several conclusions can be drawn. These are:

a) The phase-averaged spectrum of moderately (τ_T being several) deep atmospheres illuminated by soft photons gives a better fit to the 2–20 keV power law observed in X-ray pulsars than do, for instance, self-emitting atmospheres.

b) Slab models are qualitatively able to fit the observed variation of cyclotron line frequency with pulsation phase, whereas column models appear less able to do so.

c) The pulse shapes predicted by slab models are in better overall agreement with typical observed pulses than those predicted by columns.

d) A test based on pulse shapes for slab versus column models is that slabs are single-peaked at the cyclotron frequency, while columns at most viewing angles are split-pulsed (that is, at the resonance itself).

e) Slab model pulse shapes are single-peaked at the resonance but split-peaked (or triple-peaked) at the wings, $\omega_w \approx \omega_B(1 \pm 0.3)$. Columns also show split wings, but they are very strongly split at the resonance.

f) The cyclotron resonance frequency *may* be observationally identified by the presence of such split-peaked wings, which bracket the resonance itself.

REFERENCES

Basko, M. M., and Sunyaev, R. A. 1975, *Astr. Ap.*, **42**, 311.
Börner, G., and Mészáros, P. 1979, *Astr. Ap.*, **77**, 178.
Bussard, R. W., and Lamb, F. K. 1982, AIP Conf. Proc., No. 77, p. 189.
Bussard, R. W., Mészáros, P., and Alexander, S. 1985, *Ap. J. (Letters)*, **297**, L21.
Gnedin, Yu. N., and Pavlov, G. G. 1974, *Soviet Physics—JETP*, **38**, 903.
Harding, A. K., Mészáros, P., Kirk, J. G., and Galloway, D. J. 1984, *Ap. J.*, **278**, 369.
Kaminker, A. D., Pavlov, G. G., and Shibanov, Yu. A. 1982, *Ap. Space Sci.*, **86**, 249.
Kanno, S. 1980, *Pub. Astr. Soc. Japan*, **32**, 105.
Mészáros, P., and Bonazzola, S. 1981, *Ap. J.*, **251**, 695.

Mészáros, P., and Nagel, W., *Ap. J.*, **298**, 147 (Paper I).
Mészáros, P., Nagel, W., and Ventura, J. 1980, *Ap. J.*, **238**, 1066.
Nagel, W. 1980, *Ap. J.*, **236**, 904.
————. 1981*a*, *Ap. J.*, **251**, 278.
————. 1981*b*, *Ap. J.*, **251**, 288.
Pavlov, G. G., Shibanov, Yu. A., and Yakovlev, D. G. 1980, *Ap. Space Sci.*, **73**, 33.
Voges, W., Pietsch, W., Reppin, C., Trümper, J., Kendziorra, E., and Staubert, R. 1982, *Ap. J.*, **263**, 803.
White, N. E., Swank, J. H., and Holt, S. S. 1983, *Ap. J.*, **270**, 711.

PETER MÉSZÁROS: 525 Davey Laboratory, The Pennsylvania State University, University Park, PA   16802

WERNER NAGEL: Max-Planck-Institut für Astrophysik, Karl-Schwarzschildstr. 1, 8046 Garching, West Germany